On the Contribution of Grain Boundary Sliding to Firn Densification - an Assessment using an Optimisation Approach

Timm Schultz[1], Ralf Müller[1], Dietmar Gross[2], and Angelika Humbert[3,4]

[1]Institute of Applied Mechanics, Technische Universität Kaiserslautern, Kaiserslautern, Germany
[2]Division of Solid Mechanics, Technische Universität Darmstadt, Darmstadt, Germany
[3]Alfred-Wegener-Institut Helmholtz-Zentrum für Polar- und Meeresforschung, Bremerhaven, Germany
[4]Faculty of Geosciences, University of Bremen, Bremen, Germany

Correspondence: Timm Schultz (tschultz@rhrk.uni-kl.de)

Abstract. Physics based simulation approaches to firn densification often rely on the assumption that grain boundary sliding is the leading process driving the first stage of densification. Alley (1987) first developed a material model for firn describing this process. However, often so called semi empirical models are favored against the description of grain boundary sliding due to simplicity and uncertainties regarding model parameters. In this study, we are assessing the applicability of grain boundary sliding to firn using a numeric firn densification model and an optimisation approach, for which we formulate variants of the constitutive relation by Alley (1987). The efficient model implementation based on an updated Lagrangian numerical scheme enables us to perform a large number of simulations testing different model parameters, to find simulation results suiting 159 firn density profiles from Greenland and Antarctica best. For most of the investigated locations a good agreement of simulated and measured firn density profiles was found. This implies that the constitutive relation by Alley (1987) characterises the first stage of firn densification well, if suitable model parameter are used. An analysis of the parameters that lead to best matches reveals a dependency on the mean surface mass balance. This may indicate an insufficient description of the load situation, as lateral components of the stress tensor are usually neglected in one dimensional models of the firn column.

1 Introduction

Two basic categories of firn densification models can be identified. The first one, incorporating the majority of existing models, is following the so called semi empirical concept of Herron and Langway (1980), which itself is based on Sorge's Law (Bader, 1954) and the Robin Hypothesis (Robin, 1958). Examples are the models by Arthern et al. (2010), Ligtenberg et al. (2011) and Simonsen et al. (2013). Typically empirical parameters of these models are adjusted to certain datasets of depth density profiles. The second category of firn densification models tries to quantify the physical processes related to the densification of firn. These processes incorporate different types of creep and diffusion. Micro mechanical models are used for small scale investigations (Johnson and Hopkins, 2005; Theile et al., 2011; Fourtenau et al., 2020) while continuum mechanics based models can be used for large scale simulations. Examples of the latter are models by Arthern and Wingham (1998), Arnaud et al. (2000) and Goujon et al. (2003).

Alley (1987) first applied the theory of grain boundary sliding, adopted from Raj and Ashby (1971), to firn densification at densities below the critical density of $\rho_c = 550\,\mathrm{kg\,m^{-3}}$. Since then the description of this process by Alley (1987) was used in other firn densification models (Arthern and Wingham, 1998; Arnaud et al., 2000; Goujon et al., 2003; Bréant et al., 2017). Nevertheless, the assumption that grain boundary sliding is the dominant process in firn densification at densities below $\rho_c = 550\,\mathrm{kg\,m^{-3}}$ was questioned numerous times (Ignat and Frost, 1987; Roscoat et al., 2010). For example Theile et al. (2011), by conducting experiments on a small number of snow samples, suggested that the densification is more likely driven by processes within the grain than by the inter granular process of grain boundary sliding.

When Alley (1987) first published the description of grain boundary sliding for firn, he tested the material model by fitting the model results to four firn profiles available at this time, evaluating the resulting model parameters. As indicated by the title of his paper and pointed out in its discussion, grain boundary sliding might not be the only process driving the densification of firn at low density and model parameters might differ, but by using the given constitutive law it is possible to reproduce measured depth density profiles to a satisfying degree.

In this study we aim at evaluating: (i) whether grain boundary sliding and its description is suitable for the simulation of firn densification at low density, (ii) how a modification of the constitutive relation introduced by Bréant et al. (2017) affects simulation results, (iii) if hidden or additional dependencies of the constitutive relation on climatic or other conditions can be identified, and (iv) how a modification of the constitutive relation by Alley (1987), leading to improvement of the description, could look like. We want to point out that our study aims at assessing the constitutive relation for grain boundary sliding by Alley (1987). An evaluation clarifying if grain boundary sliding is the dominating process driving firn densification below the critical density of $\rho_c = 550\,\mathrm{kg\,m^{-3}}$ has to be carried out using other methods. Attempts to do so have been made for example by Kinosita (1967), Ignat and Frost (1987) and Theile et al. (2011) by conducting experiments. In contrast to these experimental investigations we follow a combination of data and physical model based approach. Since the original study by Alley (1987) was published the amount of available data became much larger. Alongside to a large number of firn profiles this includes forcing data which, together with additional modelling techniques, allows us to simulate firn profiles at a very high quality.

2 Methods

In order to test the description of grain boundary sliding by Alley (1987) we use a numeric model, simulating the evolution of a one dimensional firn column with respect to time. The model incorporates variants of the constitutive relation of Alley (1987), all of which combine several model parameters in a single factor. We then force the model with data provided by the regional climate model RACMO2.3 (Van Wessem et al., 2014; Noël et al., 2015), representing the climate of the last decades at 159 different locations where firn density measurements were retrieved. These firn measurements are available through the "Surface Mass Balance and Snow Depth on Sea Ice Working Group (SUMup) snow density subdataset" (Koenig and Montgomery, 2019). By varying the factor incorporated in the variants of the constitutive equation, we produce a large number of simulation results, which are compared to the corresponding density measurements. The quality of the factors used in the simulations is evaluated by the deviation of computed density profiles from the measured profiles. Evaluating factor values leading to best results, reveals possible improvements in the description of grain boundary sliding for firn densification at low density. In the following sections the constitutive equation for grain boundary sliding by Alley (1987), the optimisation scheme and the used density and forcing data are described. A detailed description of the model can be found in the appendix (Section A).

2.1 Grain Boundary Sliding

The different components and characteristics of the constitutive law by Alley (1987) describing the process of grain boundary sliding

$$\dot{\varepsilon}_{zz} = -\frac{2}{15} \quad \delta_b \quad \frac{8\,D_{\mathrm{BD}}\Omega}{k_b T h^2} \quad \frac{1}{r\mu^2} \quad \left(\frac{\rho_{\mathrm{ice}}}{\rho}\right)^3 \quad \left(1-\frac{5}{3}\frac{\rho}{\rho_{\mathrm{ice}}}\right) \quad \sigma_{zz} \quad , \qquad D_{\mathrm{BD}} = A_{\mathrm{BD}}\exp\left(-\frac{Q_{\mathrm{BD}}}{RT}\right) \tag{1}$$

will be explained briefly. The factor of $2/15$ results from the geometric deviation pointed out by Alley (1987). Another geometric parameter δ_b describes the width of the grain boundary.

The following part of the equation describes the reciprocal bond or boundary viscosity (Raj and Ashby, 1971). The optimisation approach of Alley (1987) aimed to find optimal values for the boundary viscosity. Alley (1987) compared the results from this optimisation to the description of the boundary viscosity by Raj and Ashby (1971), which incorporates the factor D_{BD}, the volume of the H_2O molecule Ω, the Boltzmann constant k_b, the temperature T and the amplitude of grain boundary obstructions h. The latter is a measure for the roughness of the grain boundary. D_{BD} is an Arrhenius equation describing the rate of boundary diffusion. Values for the activation energy representative for this process Q_{BD} and the corresponding prefactor A_{BD} can be found in literature (e.g. Maeno and Ebinuma, 1983, see also Section 2.2). R is the universal gas constant.

The strain rate resulting from grain boundary sliding also depends on the grain radius r. The ratio of grain radius to neck radius μ was introduced by Arthern and Wingham (1998) and is assumed to be constant. There are different methods to determine the size of grains in crystalline materials (e.g. Gow, 1969). The model by Alley (1987) was developed under the assumption of perfectly spherical grains. Although this is not true for firn, this assumption provides a reasonable basis for modelling. Therefore the grain radius r describes the radius of theoretical spherical grains throughout this study.

The next factor of Equation (1) describes the dependency on the inverse relative density to the power of three. The factor of $5/3$ corresponds to the inverse relative density of $\rho_c = 550\,\mathrm{kg\,m^{-3}}$. When the critical density and with it the theoretical densest packing of spheres is reached, the maximum coordination number of a single grain is established. At this point grains can not slide against each other any more and the process of grain boundary sliding ends. Other deformation processes, especially dislocation creep (Maeno and Ebinuma, 1983), lead to further densification with increasing stress. This behaviour is achieved in the constitutive relation by the factor incorporating the relative density ρ/ρ_{ice}. The vertical strain rate $\dot{\varepsilon}_{zz}$ decreases with increasing density ρ, until it becomes zero at the critical density ρ_c.

It has to be mentioned though, that Alley (1987) suggested also other processes leading to densification act at densities below the critical density. A decline of the strain rate due to grain boundary sliding while the influence of other processes increases, seems feasible. The studies by Arthern and Wingham (1998) and Bréant et al. (2017) use grain boundary sliding driving the densification in the first stage of firn densification exclusively. In the study by Bréant et al. (2017) the constitutive relation by Alley (1987) is changed in a way that leads to a modified transition into the second stage of densification. We will evaluate this modification throughout this study.

Finally the stress in vertical direction σ_{zz} resulting from the overburden firn is driving grain boundary sliding. While Alley (1987) used the product of the accumulation rate, acceleration due to gravity and time since the deposition of a specific firn sample to describe the overburden stress, we use a more general form at this point (see Section A2, Equation (A5)). The other physical properties influencing the process are density ρ, temperature T, and grain radius r.

2.2 Optimisation

To test the concept of the material model developed by Alley (1987) we formulate variants of Equation (1) and compare corresponding model results to density measurements of various firn cores. These variants of the constitutive equation (Equations (2) to (5)) preserve its general form, but group several material parameters into a single factor. In this way the simulation result does not depend on those parameters, but on the single factor. The factor is then varied to find an optimal simulation result recreating the measured firn profile best. The factor leading to the optimal simulation result depends on the measured firn density profile and the corresponding climate conditions. It is therefore site specific. This allows for the assessment if the description of grain boundary sliding by Alley (1987) can be used to recreate measured firn profiles under the assumption of an optimal set of parameters. It further allows to analyse the site specific factors leading to the best simulation results for possible hidden dependencies.

Arnaud et al. (2000), Goujon et al. (2003) as well as Bréant et al. (2017) also summed the material parameters of the model by Alley (1987) up into a single parameter . In the study by Bréant et al. (2017) additionally the factor of $5/3$ was modified to change the density at which the deformation due to grain boundary sliding becomes zero. In the following the four variants, indicated by the subscripts $(\cdot)_{\mathrm{v}_1}$ to $(\cdot)_{\mathrm{v}_4}$, are shown:

$$\dot{\varepsilon}_{zz\,\mathrm{v}_1} = -C_{\mathrm{v}_1}\, D_{\mathrm{BD}} \frac{1}{T}\frac{1}{r}\left(\frac{\rho_{\mathrm{ice}}}{\rho}\right)^3 \left(1 - \frac{5}{3}\frac{\rho}{\rho_{\mathrm{ice}}}\right)\sigma_{zz} \quad , \qquad D_{\mathrm{BD}} = A_{\mathrm{BD}} \exp\left(-\frac{Q_{\mathrm{BD}}}{RT}\right), \tag{2}$$

$$\dot{\varepsilon}_{zz\,\mathrm{v}_2} = -C_{\mathrm{v}_2}\, D_{\mathrm{BD}} \frac{1}{T}\frac{1}{r}\left(\frac{\rho_{\mathrm{ice}}}{\rho}\right)^3 \left(1 + \frac{0.5}{6} - \frac{5}{3}\frac{\rho}{\rho_{\mathrm{ice}}}\right)\sigma_{zz} \quad , \qquad D_{\mathrm{BD}} = A_{\mathrm{BD}} \exp\left(-\frac{Q_{\mathrm{BD}}}{RT}\right). \tag{3}$$

Variant 1 (Equation (2)) and Variant 2 (Equation (3)) of the constitutive equation combine all material constants using the factors C_{v_1} and C_{v_2}, respectively. The Arrhenius equation for boundary diffusion D_{BD} (see Equation (1)) is preserved in these variants. Following Maeno and Ebinuma (1983) we use a value of $Q_{\mathrm{BD}} = 44.1\,\mathrm{kJ\,mol^{-1}}$ for the boundary diffusion activation energy. It is defined by Maeno and Ebinuma (1983) by two thirds of the activation energy for lattice diffusion measured by Itagaki (1964). The corresponding prefactor is $A_{\mathrm{BD}} = 3.0 \times 10^{-2}\,\mathrm{m^2\,s^{-1}}$. Alley (1987) assumed a similar value for the boundary diffusion activation energy.

Except for the temperature T, the vertical strain rate $\dot{\varepsilon}_{zz}$ only depends on the firn density ρ, the grain radius r and the stress in vertical direction σ_{zz}. Variant 2 differs from Variant 1 by the use of the modification introduced by Bréant et al. (2017). This modification leads to a theoretical ending of the process of grain boundary sliding at the density of $\rho_c^* = 596\,\mathrm{kg\,m^{-3}}$. It was introduced to grant better transition into the second stage of firn densification. The strain rate due to grain boundary sliding is therefore higher at the critical density when using the modification.

To test the influence of the Arrhenius law it is disregarded in Variants 3 and 4 as shown in Equations (4) and (5):

$$\dot{\varepsilon}_{zz\,\mathrm{v}3} = -C_{\mathrm{v}3} \frac{1}{T} \frac{1}{r} \left(\frac{\rho_{\mathrm{ice}}}{\rho} \right)^3 \left(1 - \frac{5}{3} \frac{\rho}{\rho_{\mathrm{ice}}} \right) \sigma_{zz} \,, \tag{4}$$

$$\dot{\varepsilon}_{zz\,\mathrm{v}4} = -C_{\mathrm{v}4} \frac{1}{T} \frac{1}{r} \left(\frac{\rho_{\mathrm{ice}}}{\rho} \right)^3 \left(1 + \frac{0.5}{6} - \frac{5}{3} \frac{\rho}{\rho_{\mathrm{ice}}} \right) \sigma_{zz} \,. \tag{5}$$

Again in Variant 4 the modification by Bréant et al. (2017) is used while Variant 3 incorporates the original formulation by Alley (1987).

The aim of the optimisation is to find optimal values of the factors C_{v} for every variant of the constitutive relation (Equations (2) to (5)) resulting in a simulated density profile that represents the measured profiles in the best possible way. As an example, we explain the optimisation process for one selected firn core in more detail. The upper part of ice core ngt03C93.2 (Wilhelms, 2000) is shown in Fig. 1 (a).

Every simulation starts with a spin up in which constant values are used for the forcing. When steady state is reached, a transient run using evolving forcing data follows. The forcing at the location of ngt03C93.2 is shown in Fig. 1 (c). The resulting firn profile is then compared to the measured profile. We use the root mean square deviation between measured and modelled density for comparison, which allows a simple and easy to compute comparability between the simulation result and the density measurement. To calculate the deviation, simulated density values are interpolated linearly to the measurement locations along the profile. To guarantee a high quality of the results, we restrict the calculation of the deviation to the domain defined by the the location of the uppermost available measurement point and the oldest horizon within the firn profile affected by the forcing. In case of ngt03C93.2 this horizon is the surface of 1958 at a depth of approximately $11\,\mathrm{m}$ below the surface, indicated by dashed horizontal lines in Fig. 1 (a). Only results located above the surface of 1958 are incorporated in the calculation of the deviation. Examining other firn cores, the surface of the oldest available forcing may be located at greater depth, when a density of $\rho_c = 550\,\mathrm{kg\,m^{-3}}$ is already reached. In those cases the computation of the root mean square deviation is restricted to the domain showing density values smaller than $540\,\mathrm{kg\,m^{-3}}$. We decided to use a smaller density threshold than the critical density due to the asymptotic characteristic of the resulting density profiles using Variants 1 and 3 of the constitutive equation (Equations (2) and (4)). The value of $540\,\mathrm{kg\,m^{-3}}$ rendered to ensure comparability between results of the different variants of the constitutive relation while unique values for the factors C_{v} were found quickly throughout the optimisation.

As the implementation of our model is efficient and the approach is as well simple and reliable, we decided to determine the best factor C_{v} for the four variants of the constitutive equation, by simply testing 250 values within certain ranges. These ranges are shown in Equations (6) and (7). They differ because of the inclusion or disregard of the Arrhenius law, respectively.

Optimal factors can be found within these range boundaries for every analysed firn profile. To ensure this, all simulations were performed multiple times testing different ranges of factors.

$$1.0\times10^{-9}\,\mathrm{K\,s^2\,kg^{-1}} \quad \leq C_{\mathrm{v_1,v_2}} \leq \quad 2.5\times10^{-4}\,\mathrm{K\,s^2\,kg^{-1}} \tag{6}$$

$$2.5\times10^{-21}\,\mathrm{K\,s\,m^2\,kg^{-1}} \quad \leq C_{\mathrm{v_3,v_4}} \leq \quad 5.0\times10^{-15}\,\mathrm{K\,s\,m^2\,kg^{-1}} \tag{7}$$

Figure 1 (b) shows the root mean square deviation (RMSD) plotted over the 250 tested values for the four different factors. The different variants are color coded and the best result is marked. The smallest value of the deviation is shown within the figure. The corresponding density profiles are shown in Fig. 1 (a).

As can be seen in Fig. 1 (a) the firn profile of ngt03C93.2 starts at a depth of about $1.3\,\mathrm{m}$. This yields the problem of finding an appropriate surface density, needed as boundary condition in the simulation. As firn density profiles differ greatly especially near the surface the derivation of an appropriate surface density is difficult. Following our approach we tested 21 different values for the surface density between $\rho_0 = 250\,\mathrm{kg\,m^{-3}}$ and $\rho_0 = 450\,\mathrm{kg\,m^{-3}}$, using steps of $\Delta\rho_0 = 10\,\mathrm{kg\,m^{-3}}$. Afterwards the best result is chosen. This method proofed to work well throughout the study. Firn profiles which start at small depths, providing near surface density data are well represented. Applying the method to all firn profiles no matter at which depth they begin, accounts for comparability of the results. Overall $4\times250\times21 = 21\,000$ simulations were performed in case of ice core ngt03C93.2 to find the optimal results shown in Fig. 1.

3 Data

3.1 Firn Profiles

In order to test the description of grain boundary sliding by Alley (1987), we use 159 firn profiles of which 80 were retrieved in Greenland. The remaining 79 measurements were taken in Antarctica. The profiles are included in the "Surface Mass Balance and Snow Depth on Sea Ice Working Group (SUMup) snow density subdataset" (Koenig and Montgomery, 2019). Individual references for all 159 firn profiles are listed in the supplementary material. The dataset does not feature the four profiles used in the study by Alley (1987), as the original data of these firn cores are unpublished. To obtain firn profiles relevant for this study from the dataset, we filter it based on the following conditions:

1. Profiles have to consist of at least ten data points.
2. The overall length of the profiles has to exceed three meters.
3. Profiles have to start at a depth of less than three meters below surface.
4. The starting density of the profiles must not to exceed $\rho_c = 550\,\mathrm{kg\,m^{-3}}$.

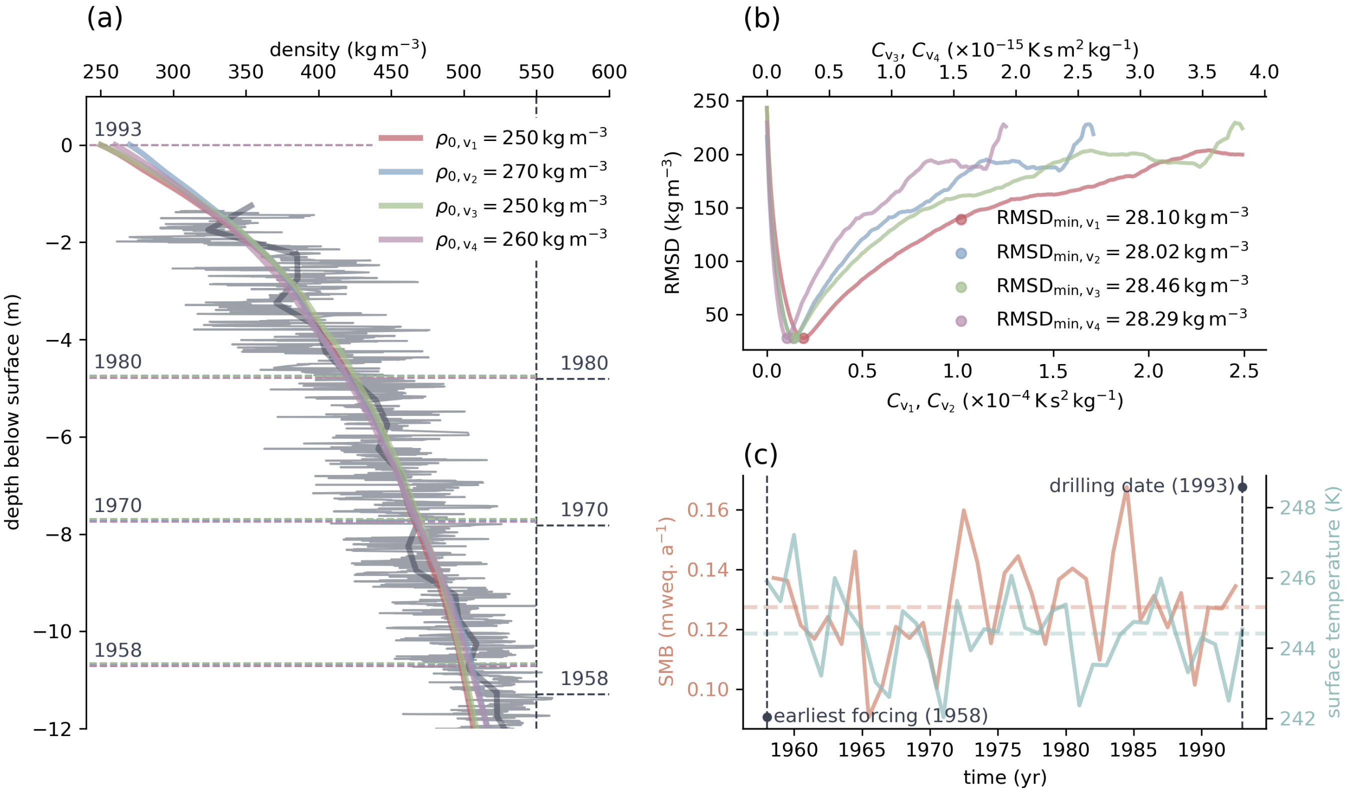

Figure 1. Panel (a) of the figure shows the depth density profile of ice core ngt03C93.2 (Wilhelms, 2000) retrieved in Greenland in gray colour and the best corresponding model results using four different variants of the constitutive law for grain boundary sliding by Alley (1987) in different colors. The strong gray line shows the mean density of the ice core calculated using a window of $0.5\,\mathrm{m}$, starting at the surface. Dashed horizontal lines represent horizons of firn deposited in the indicated years, 1958 being the first year forcing from RACMO2.3 (Van Wessem et al., 2014; Noël et al., 2015) is available. Simulation results are drawn using colors as shown in the legend. Horizons plotted in gray, right of the vertical dashed line, represent the same surfaces as determined by Miller and Schwager (2004) during analysis of the core. Panel (b) shows the root mean square deviation between measured and modelled density plotted over the range of tested factor values. Note the different axes for different tested factors. The forcing representative for the location of ice core ngt03C93.2 and used in the simulation is shown in panel (c). Horizontal dashed lines show the mean values of the surface mass balance and surface temperature over the course of the simulation time.

5. The surface mass balance at the profile locations has to be positive.
6. Forcing data of at least five years have to be available for the profile location.

While criteria 1. and 2. ensure general quality of the data, conditions 3. and 4. guarantee the first stage of firn densification is incorporated. As the model is not capable of handling melt and the study focuses on dry firn densification, the surface mass balance should be positive as stated in the fifth criterion. However, a positive mean annual surface mass balance does not guarantee no melt occurs over the course of a year. Based on the data available for this study a distinction between sites influenced by melt and sites where no melt occurs is not possible. The number of these sites however is expected to be small in comparison to the overall number of analysed firn profiles. Due to the method their influence on the overall result is therefore small. Forcing data comes from the regional climate model RACMO2.3 (Van Wessem et al., 2014; Noël et al., 2015). This provides the surface mass balance. The model delivers data for times from 1958 to 2016 and 1979 until 2016 for Greenland and Antarctica, respectively (see also Section 3.2). Density measurements used for model comparison should thus be retrieved during this periods. We chose to only use datasets for which at least five years of forcing data is available. Furthermore a number of density profiles were excluded from the filtered data by hand. This incorporates profiles with very low spatial resolution, atypical profiles showing decreasing density with depth and measurements with a surface density very close to the critical density of $\rho_c = 550\,\mathrm{kg\,m^{-3}}$. As explained in Section 2.2 and illustrated in Fig. 1, we only use a certain domain for the comparison between simulated and measured data. If this domain turns out to be less than $2.5\,\mathrm{m}$ long in case of any of the tested variants of the constitutive equation, the firn profile in question is neglected in the further analysis.

Figure 2 illustrates the locations from which the 159 density profiles were retrieved. The 80 measurements from Greenland are relatively uniformly distributed over the ice sheet. Coastal locations are not well covered due to the requirement of a strictly positive surface mass balance. In the Antarctic sites in east Antarctica are underrepresented. However a wide variety of environments is covered, including the Filchner-Ronne Ice Shelf, the west Antarctic coast and Dronning Maud Land.

3.2 Boundary Conditions and Forcing

To force the firn densification model, surface values for density, temperature, accumulation rate and grain radius at the locations of the 159 firn profiles are needed. Although Alley (1987) used constant forcing we follow the example of Arthern and Wingham (1998) and Goujon et al. (2003) performing transient simulations.

As measured firn density profiles represent past climate conditions, the choice of forcing data is crucial for the presented method. Uncertainties in the forcing will reflect in the simulation results and therefore in the comparison with measured firn profiles. Neither the model formulation nor the optimisation scheme can compensate for that. We use data provided by the regional climate model RACMO2.3 (Van Wessem et al., 2014; Noël et al., 2015)5. RACMO2.3 provides forcing data for the Greenland ice sheet covering the period from 1958 to 2016. In case of Antarctica the time period is shorter, starting in 1979 and ending in 2016. Data for the mean annual skin temperature and surface mass balance for the Greenland ice sheet are available at mean spatial resolutions of $11.3\,\mathrm{km}$ and $1.0\,\mathrm{km}$ respectively for this study. Mean spatial resolutions for Antarctica are $8.0\,\mathrm{km}$ and $28.5\,\mathrm{km}$ for mean annual skin temperature and surface mass balance. Spatial interpolation of the fields obtained

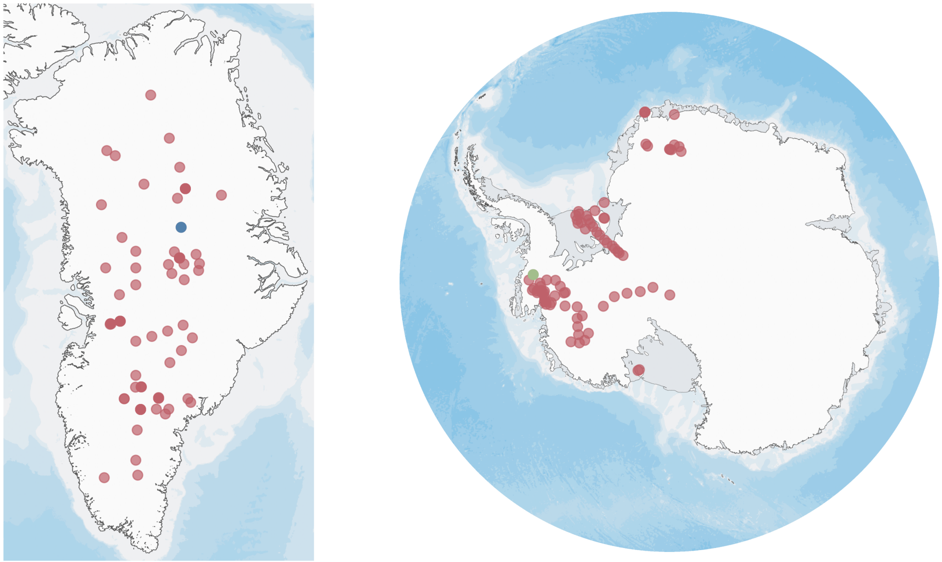

Figure 2. Locations of the firn profiles used for model comparision. 80 profiles were measured in Greenland, 79 depth density datasets were retrieved in Antarctica. The blue marker shows the location of ice core ngt03C93.2 (Wilhelms, 2000, N 73.940°, E -37.630°). The green marker shows the location of site 3 of the iSTAR traverse from which the firn core shown in Figure 3 was retrieved (Morris et al., 2017, N -74.565°, E -86.913°). Map data: Amante and Eakins (2009); Arndt et al. (2013), SCAR Antarctic Digital Database.

from RACMO2.3 output leads to forcing data for the locations of the investigated firn profiles. It has to be mentioned that such an interpolation may introduce systematic errors.

The time period for transient simulation runs, as described in Section 2.2, is specified by the earliest data available from RACMO2.3 and the drilling date of the firn core under consideration. In case of ice core ngt03C93.2 (Wilhelms, 2000), which was retrieved in central Greenland in 1993, the simulation time covers the period from 1958 to 1993 (see Fig. 1 (c)). Constant values of the surface temperature and surface mass balance for the preceding spin up are calculated as mean values over this time range.

Using a second example we want to illustrate how the temporal resolution of the forcing affects the optimisation results and why we decided to use yearly averaged data provided by RACMO2.3. Figure 3 shows the depth density profile of the firn core retrived at site 3 of the iSTAR Traverse in 2013 (Morris et al., 2017). The location of the site at Pine Island Glacier in West Antarctica is shown in Fig. 2. Instead of using forcing data from RACMO2.3, for this particular simulation we used "ERA5-Land monthly averaged data from 1981 to present" (Muñoz Sabater, 2019; Hersbach et al., 2020), as it is freely available at monthly resolution. From this data we computed annual average data for a second simulation run. The forcing data at both resolutions is shown in Fig. 3 (c). Panel (a) of the figure shows the best simulated firn profiles identified using the optimisation approach in comparison with the measured density profile. On the left hand side results using the annually averaged forcing data are shown, while the right hand side illustrates the results using monthly averaged data from ERA5. In case of the higher

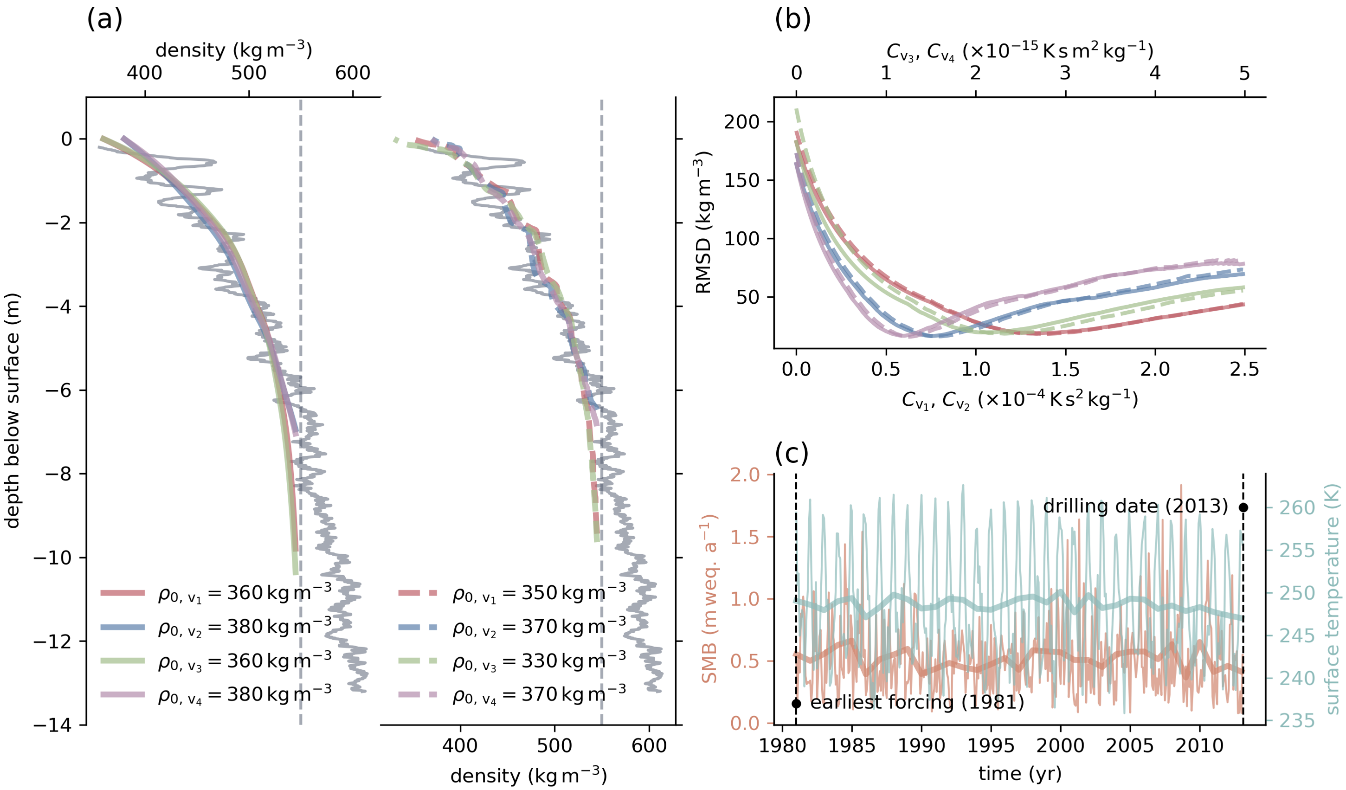

Figure 3. Panel (a) of the figure shows the depth density profile of the firn core retrieved at site 3 of the iSTAR traverse (Morris et al., 2017) in gray colour. Colour coded the optimised simulation results for all four variants of the constitutive relation are pictured. The simulated density profiles on the left result from yearly averaged surface forcing while the profiles on the right, plotted using dashed lines, result from monthly averaged forcing. In panel (b) the root mean square deviation (RMSD) between the best simulation result and the measured firn profile is shown over the range of tested optimisation factors C_v. Colours again indicate results for the different variants of the constitutive relation. Dashed lines are used for results computed with monthly averaged forcing while solid lines indicate the use of yearly averaged surface forcing. The forcing data from "ERA5-Land monthly averaged data from 1981 to present" (Muñoz Sabater, 2019; Hersbach et al., 2020) is shown in panel (c) from the earliest available forcing in 1981 to the date the firn core was drilled in 2013. Strong lines show the yearly averaged data computed from the monthly averaged data.

resolution data much more detail is covered within the simulated firn density profiles. However, the aim of this study is not primarily to reproduce the analysed measured firn profiles with highest possible detail, but to evaluate the constitutive relation by Alley (1987) using an optimisation approach finding site specific optimal constitutive factors C_v (see Section 2.2). Panel (b) of Fig. 3 shows the root mean square deviation of the simulated profiles from the measured profile over the range of tested optimisation factors. Dashed lines belong to the simulations performed using the high resolution forcing data, while solid lines are dedicated to the annual averaged data. The difference between the optimisation results is small. We therefore decided to use annual averaged data provided by RACMO2.3, available for this study, as the data covers, especially for Greenland, a greater time period. This allows us to analyse more firn profiles at greater detail. In case of ice core ngt03C93.2 (Wilhelms, 2000) the horizon of the year 1981, the earliest forcing available in ERA5, lies at a depth of about $5\,\mathrm{m}$ below surface as can be seen in Fig. 1 (a). The horizon of the earliest forcing available by RACMO2.3, the year 1958, is located at a depth of about $11\,\mathrm{m}$ below surface. A much greater part of the simulated firn profile is therefore influenced by the surface forcing. Furthermore the use of yearly averaged data produces less overhead.

As pointed out in Section 2.2 we use 21 surface density values in the range of $250\,\mathrm{kg\,m^{-3}} \leq \rho_0 \leq 450\,\mathrm{kg\,m^{-3}}$ for every tested firn profile. The value leading to the best result is then used for further analysis. Due to the lack of relevant data, simplicity and better comparison options the grain radius at the surface is assumed to be the same at all location and to be constant over time. We chose to use a grain radius of $r_0 = 0.5\,\mathrm{mm}$ based on the measurements and empirical relation by Linow et al. (2017) and the assumption of Arthern and Wingham (1998). As climatic conditions and therefore the surface grain size differ at every investigated location this is a simplification. Due to the optimisation approach the influence of this parameter is of less significance as it can be understood as a constant part of the grain radius, which is the same for every analysed firn profile.

Figure 4 illustrates the range and distribution of surface boundary conditions at the investigated sites. In comparison locations in Greenland show a higher mean surface temperature and surface mass balance than locations in Antarctica. The surface density is higher at Antarctic location than those in Greenland. In general a wide variety of typical climatic conditions for both ice sheets is covered.

3.3 Distribution and Influence of Input Data

Ice core ngt03C93.2 shown in Fig. 1 (a) is an example of a high resolution density measurement showing extensive small scale layering. Only few of the 159 firn profiles are of such high quality and cover such kind of layering. Although our model approach works on a high temporal and spatial resolution, it does not cover layering as shown in Fig. 1 (a). Simulation of small scale layering could easily be added to the model following the approach of Freitag et al. (2013), introducing a dependency of the activation energy Q_BD for the process of boundary diffusion (Equation (1)) on a proxy for impurities. Such data are not globally available. The activation energy can therefore be understood as a temporally averaged value, leading to a mean density. The use of the root mean square deviation for comparison of simulation results and measured density profiles assures the optimisation result is independent of layering. To illustrate this the running mean density of ice core ngt03C03.2 is shown

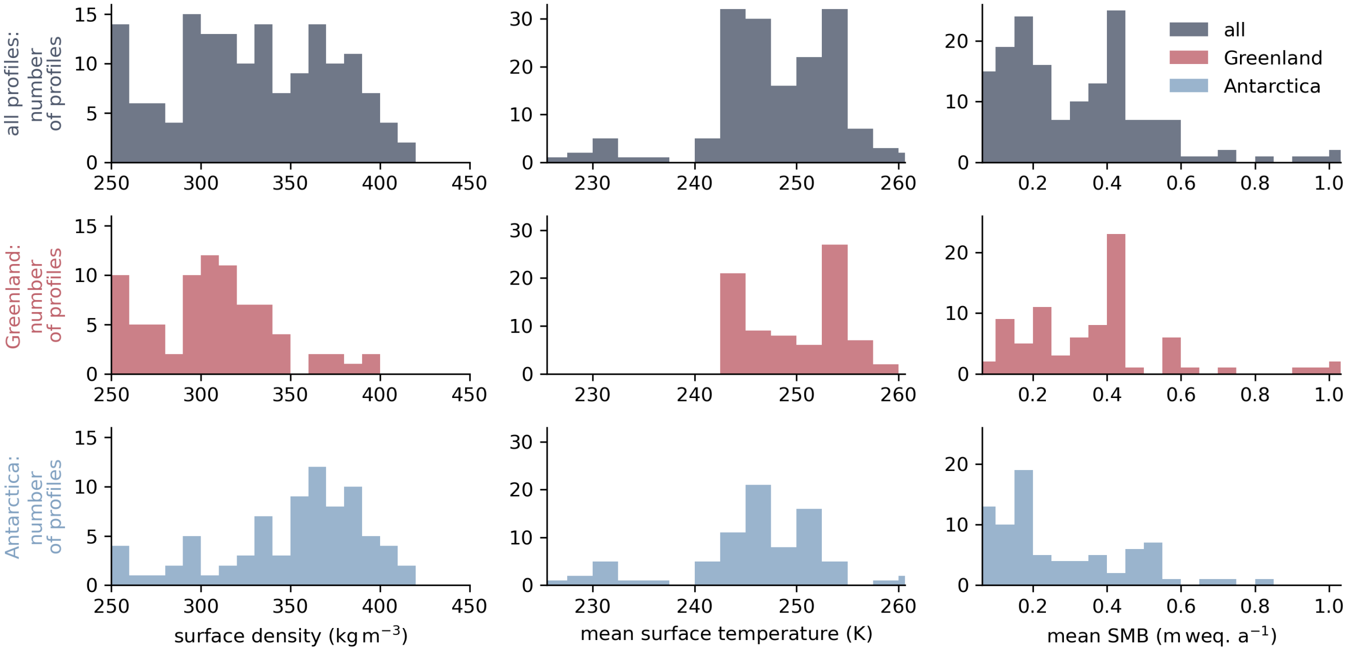

Figure 4. Distribution and comparison of the boundary conditions at the 159 firn profile sites. All values are averaged over the specific simulation time for every location, beginning in the year 1958 or 1979 respectively and ending at the date of measurement (see Section 3.2). The top row of plots, in gray colour, shows the boundary conditions at all locations, while the middle and bottom row, in red and blue, exclusively represent locations in Greenland and Antarctica. Data for the surface temperature in the middle, and surface mass balance in the right column, are provided via RACMO2.3 (Van Wessem et al., 2014; Noël et al., 2015).

in Fig. 1 (a). Note that computing the running mean neglects information. Thus we compute the root mean square deviation on the basis of the original data.

In this study we focus on the very first stage of firn densificaiton and the upper most meters of the firn column. We limit the model domain to a maximum depth of $-25\,\mathrm{m}$ below surface. Furthermore we do not develop the density further after the critical density of $\rho_c = 550\,\mathrm{kg\,m^{-3}}$ is reached. This raises the question if the use of a Neumann boundary condition at the profile base to solve for the temperature as described in Section A4 is justified for this particular model setup. The critical density of $\rho_c = 550\,\mathrm{kg\,m^{-3}}$ is mostly reached within the upper ten meters of the firn column. The temperature within this domain is influenced by the surface conditions, covered by the forcing data. At greater depths the temperature corresponds to the mean annual surface temperature and changes very little (e.g. Cuffey and Paterson, 2010, pp. 399 ff.). The amount of high resolution temperature measurements in firn is sparse. Orsi et al. (2017) published a temperature profile of $147\,\mathrm{m}$ length from borehole NEEM2009S1, which shows a temperature difference of little more than $1\,\mathrm{K}$ over the entire profile. The study by Vandecrux et al. (2021) suggests the same. Such small temperature change, below the depth of approximately $10\,\mathrm{m}$ below the surface has little effect on our model approach. To test the sensitivity of the optimisation approach on the temperature we performed reruns of the simulations with the site specific surface temperature forcing increased and decreased by $1\,\mathrm{K}$. The effect on the optimal factors C_v differs depending on the variant of the constitutive relation, but in general is small. For example the greatest difference between the optimal factors resulting from the correct and the adjusted forcing in case of ice core ngt03C93.2 (Wilhelms, 2000) can be found when using Variant 1. It shows a value of $\Delta C_{\mathrm{v1,\,max}} = 0.02 \times 10^{-4}\,\mathrm{K\,s^2\,kg^{-1}}$, which corresponds to two times the sampling space of the factors C_{v_1} used in the optimisation. In case of Variant 4 the results are even the same. Because of this small influence in general, the greater influence of the surface temperature in the investigated domain and the restriction of the comparison to the domain actually influenced by the surface forcing a Neumann boundary condition at the profile base, despite the low depth, is justified.

4 Results

Figure 5 illustrates the distribution of the root mean square deviation (RMSD) calculated from the simulated firn profiles matching the measured profiles best. The four different plots of the figure distinguish between the four different variants of the constitutive equation for grain boundary sliding (Equations (2) to (5)) as described in Section 2.2. Additionally the median value of the data is shown. The differences in the distribution of the deviation are small with regard to the different tested variants. The median values differ in a small range. Variant 2 shows the smallest value and Variant 3 the greatest. The use of the modification introduced by Bréant et al. (2017) within the constitutive equation results in $6.2–6.8\,\%$ better agreement between simulated and measured firn profiles. To put the values in perspective, the deviation of the four best fitting modelled firn profiles from ice core ngt03C93.2 (Wilhelms, 2000) displayed in Fig. 1 is about $28\,\mathrm{kg\,m^{-3}}$. That means, more than half of the resulting simulations show even better agreement with the corresponding firn density profiles than this one. An overview of the deviation between all 159 measured firn profiles and the corresponding best simulation results can be found in the supplementary material.

The range of factors resulting in the best fitting firn profile is smaller for Variants 2 and 4 of the constitutive equation, which use the modification by Bréant et al. (2017), compared to Variants 1 and 3, as shown in form of box plots in Fig. 6. In contrast to factors C_{v_1} and C_{v_2}, factors C_{v_3} and C_{v_4} incorporate the Arrhenius law from the original description of grain boundary sliding by Alley (1987). Therefore a direct comparison between the two groups of factors is not possible. The quartile coefficient of dispersion, shown for the four variants on the right side of Fig. 6, is a relative measure for the scatter of the values. The coefficient reveals that the resulting factors of Variants 1 and 2 are defined in a range narrower versus Variants 3 and 4. All four resulting sets of factors show a slightly non uniform distribution, tending towards smaller values.

To find a possible dependency of the resulting factors, leading to the best match between simulated and measured density profiles, Fig. 7 shows the 159 factors found by the optimisation, plotted against the mean surface temperature calculated from the forcing data specific for each firn profile's site. The left plot illustrates the results for Variants 1 and 2 in red and blue colour, while the right part of the figure shows the resulting factors for Variants 3 and 4 using green and purple markers, respectively. The legend features the Pearson correlation coefficient r_Pearson, a measure for the linear correlation of the two variables, and the distance correlation $dCor$ (Székely et al., 2007). The distance correlation was designed by Székely et al. (2007) to overcome

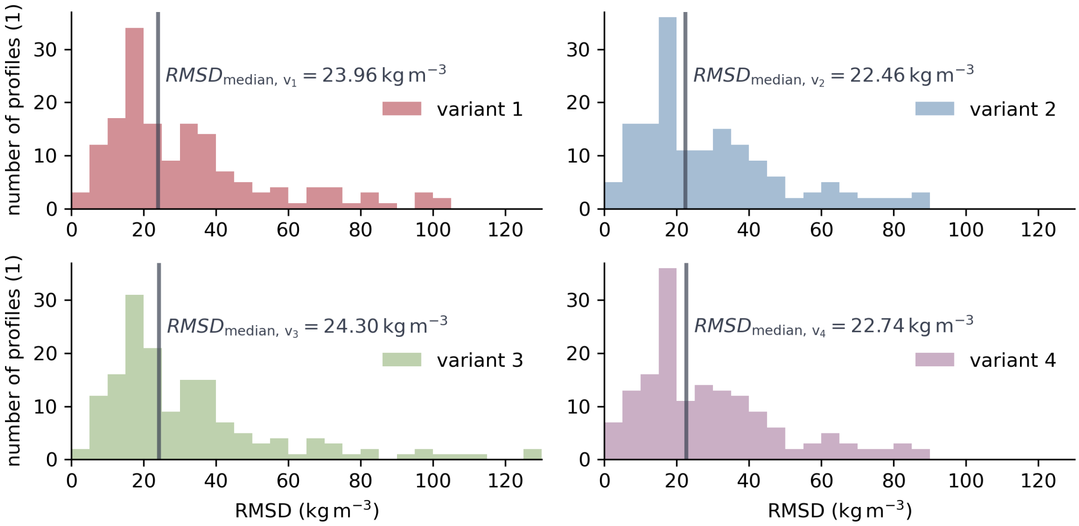

Figure 5. Distribution of the smallest root mean square deviation (RMSD) for every analysed firn profile found using the optimisation scheme outlined in Section 2.2. The four plots show the results for the four tested variants of the constitutive equation. Vertical lines illustrate the median value of the 159 values.

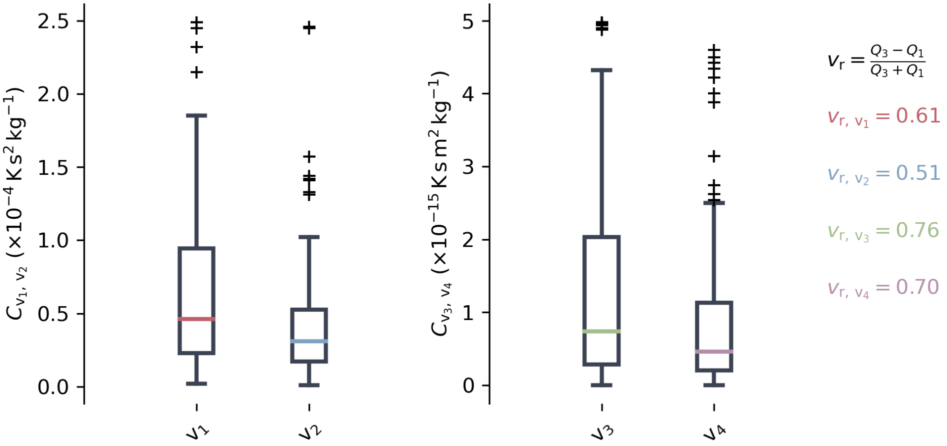

Figure 6. Box plots showing the distribution of the best factors C_{v_1} to C_{v_4} for the four variants of the constitutive equation describing grain boundary sliding (see Equations (2) to (5)), derived using the optimisation scheme described in Section 2.2. On the right side the quartile coefficient of dispersion v_r is shown for the variants in corresponding colors. The quartile coefficient of dispersion is calculated using the first Q_1 and third Q_3 quartile values of the data sets as shown in black colour and represents a robust relative measure of dispersion.

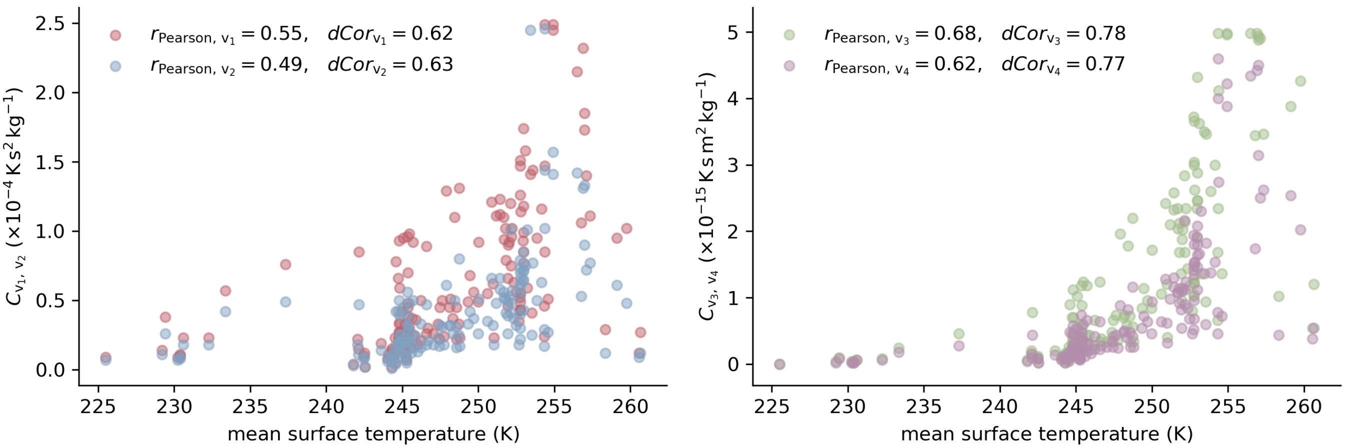

Figure 7. Best factors for every investigated firn profile, determined using the optimisation scheme, plotted against the mean surface temperature during the forcing period (see Section 4). On the left side of the figure the results for Variants 1 and 2 of the constitutive equation are shown in blue and red colour respectively, while the right plot illustrates the results of Variants 3 and 4 in green and purple colours. The Pearson correlation coefficient r_{Pearson}, representing the linear correlation between factors C_{v_1} to C_{v_4} and the mean surface temperature, as well as the distance correlation $dCor$ are given within the legend.

problems of the Pearson correlation coefficient. It describes the correlation of two vectors while not being restricted to linear dependency. It is defined in the range between zero and one, where zero indicates independence of the variables.

The correlation of the resulting factors with the mean surface temperature is higher compared to other properties. This is especially true for factors C_{v_3} and C_{v_4} of Variants 3 and 4. However, the Pearson correlation coefficient only indicates the linear correlation. The scatter of factors C_{v_3} and C_{v_4} with respect to the mean surface temperature might resemble a higher order function as indicated by the higher values of the distance correlation.

Values of the Pearson correlation coefficient and distance correlation shown in Fig. 8 are higher than in Fig. 7. The figure shows the resulting factors in the same manner as Fig. 7 but with respect to the mean surface mass balance. Just as the mean surface temperature, the mean surface mass balance is calculated from the forcing data used during the simulations. The correlation coefficients for the results of Variants 3 and 4 exceed the ones for the variants of the constitutive equation incorporating the Arrhenius law explicitly. The best indication of a relationship between the factor resulting in the density profile best matching the corresponding field measurement and the surface mass balance can be seen for Variant 3.

A striking feature within Fig. 8 can be found around a mean surface mass balance of $0.4\,\mathrm{m\,weq.\,a^{-1}}$. Values of the factors resulting in the best match between simulation results and measured density profiles show a wide range for all four variants of the constitutive relation. The corresponding profiles are part of a study by Harper et al. (2012) which took place in western Greenland. The study region is relatively small which explains the similar climatic conditions. Although the mean annual surface mass balance is positive, melting occurs throughout the year influencing the firn density.

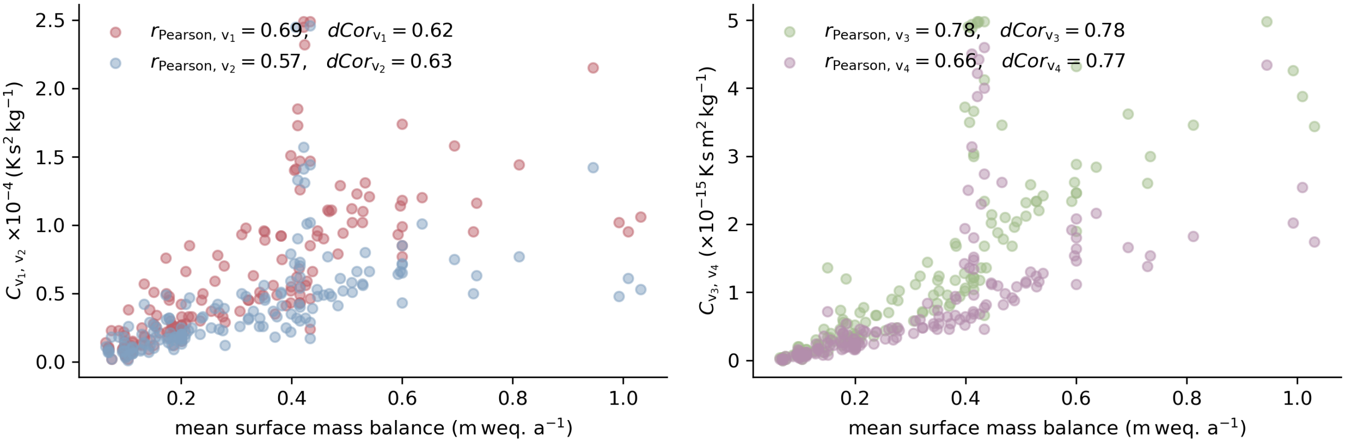

Figure 8. Resulting factors of the optimisation over the mean surface mass balance, calculated for everyone of the 159 firn profiles from its forcing. The left hand side plot shows best fitting values for factors C_{v_1} and C_{v_2}. The plot on the right shows the corresponding values for Variants 3 and 4 or factors C_{v_3} and C_{v_4} respectively. The linear correlation between factors and mean surface mass balance is illustrated by the Pearson correlation coefficient r_{Pearson} and the general correlation by the distance correlation $dCor$.

5 Discussion

Using the four variants of the constitutive relation by Alley (1987) (Equations (2) to (5)) we were able to generate density profiles matching most of the 159 density measurements well. Uncertainties may arise from the forcing, the limited knowledge on initial grain radius and the poor constraint on density at the surface. As measured firn densities represent past climate conditions, deviant forcing would always result in a mismatch between simulated and measured firn properties, independent of the optimisation approach and physical model. However, the presented optimisation scheme leads to distinct minima of the deviation between simulated and measured density profiles, indicating the forcing represents the climatic history of the firn profiles in principle.

The optimisation scheme results in site specific values for the factors C_{v_1} to C_{v_4}. As the optimisation is specific for the analysed site and variant of the constitutive relation, the four simulated density profiles for one specific site are very similar, as is illustrated in Fig. 5. This allows us to compare the factors resulting from the four variants. The differences between the factors do not primarily arise from differences in the simulated density profiles, but reflect the differences in the variants, leading to almost the same result.

However, due to the principle of the optimisation scheme possible errors included in the forcing data or other parameters like the activation energy used for the computation of the grain radius (see Equation A11) are also included in the site specific optimal factors C_{v_1} to C_{v_4}. If for example the surface temperature forcing at a site is constantly off by five degree Kelvin over the simulation time, this can be compensated by a corresponding adjustment of the specific optimisation factor C_{v} (see also Section 3.3). However, the great amount of analysed firn profiles compensates for such random error. Systematic error included in the forcing data can not be identified. Therefore, improvements of the forcing with respect to resolution in time and covering of longer periods, could lead to better and more detailed simulation results in future as is shown in Fig. 3.

It should be mentioned again that we have not investigated whether grain boundary sliding is indeed the dominating process during the first stage of firn densification. We assess whether a process with a functional dependence on density, firn overburden stress, temperature and grain radius, is representing observed density profiles well. Any other deformation process with the same functional dependence would be equally well suited. Nevertheless, by maintaining the general structure of the constitutive relation by Alley (1987), we conclude that this description of grain boundary sliding is a good basis for a physically based model describing firn densification up to the critical density of $\rho_c = 550\,\mathrm{kg\,m^{-3}}$.

Comparing the results for Variants 1 and 2, as well as Variants 3 and 4, we find that the adjustment of $\left(1 - \frac{5}{3}\,\rho/\rho_{\mathrm{ice}}\right)$ to $\left(1 + \frac{0.5}{6} - \frac{5}{3}\,\rho/\rho_{\mathrm{ice}}\right)$ is leading to better matches with measured density profiles. With regard to the study design and the background of a physics based model describing firn densification, this result has to be reviewed carefully. As Alley (1987) points out, grain boundary sliding might be the dominant process driving the firn densification at low densities, but presumably not the only one. The constitutive law by Alley (1987) is designed in a way that the densification due to grain boundary sliding becomes zero at the density of $\rho_c = 550\,\mathrm{kg\,m^{-3}}$, motivated by densest packing of spheres and increasing accommodation incompatibilities. The modification by Bréant et al. (2017) changes this behaviour in the way that the process grain boundary sliding vanishes at a density of about $\rho_c^* = 596\,\mathrm{kg\,m^{-3}}$, which could have advantages for the transition into the next stage of firn densification. We suggest a simultaneous decline of grain boundary sliding and increase of one or more other processes would provide a good characterisation. Namely dislocation creep drives the densification at higher density (Maeno and Ebinuma, 1983) due to increasing stresses. An onset of dislocation creep at densities lower than $\rho_c = 550\,\mathrm{kg\,m^{-3}}$ affecting not necessarily the entire bulk firn matrix, but increasing volume fractions of the porous matrix should be investigated further in future.

Variants 1 and 2 of the constitutive relation by Alley (1987) incorporate the Arrhenius equation for boundary diffusion D_{BD} from the description of the bond viscosity by Raj and Ashby (1971). For the formulation of Variants 3 and 4 we neglected the Arrhenius equation. As can be seen in Fig. 5, the difference in the resulting root mean square deviation is small, whether the Arrhenius equation D_{BD} is considered or not. This is consistent as we determine individual factors C_{v} for every site. The similarity of the results allows us to compare factors C_{v_1} and C_{v_2}, which were determined including the Arrhenius equation D_{BD}, to factors C_{v_3} and C_{v_4}, resulting from the variants of the constitutive relation without the Arrhenius equation. As the Arrhenius equation D_{BD} is a function of temperature it is reasonable to take a look at the dependency of the factors on the mean surface temperature as shown in Fig. 7.

The determined factors C_{v_3} and C_{v_4}, resulting from variants without the Arrhenius equation for boundary diffusion D_{BD}, show a stronger dependency on the mean surface temperature than factors C_{v_1} and C_{v_2}. At the same time, factors C_{v_1} and C_{v_2} show less dispersion than factors $C_{\mathrm{v}3}$ and C_{v_4}, as is shown in Fig. 6. The inclusion of the Arrhenius equation D_{BD} in the constitutive relation leads to better determination of these factors. It is therefore a meaningful description within the constitutive relation. Although the inclusion of the Arrhenius equation results in better determination of factors C_{v_1} and C_{v_2}, we still see a dependency on the mean surface temperature to some degree. A better determination of the parameters of the Arrhenius equation may result in resolving this dependency. If this is not the case another dependency on the temperature may be introduced to improve the constitutive relation for grain boundary sliding.

We interpret the dependency on the surface mass balance such, that the load situation is currently not represented well. The stress is represented by a second order tensor. A firn column represented in a one dimensional modelling approach would be surrounded by neighbouring firn columns, a lateral confinement restricting deformation in horizontal direction. The horizontal components of the stress tensor are not zero. As firn is a compressible material, the determination of these horizontal stress components is not trivial. The frequently used term "overburden pressure" is misleading as the mechanical pressure is defined as the spherical part of the Cauchy stress tensor (e.g. Haupt, 2002, p. 301) and is not in general identical to the normal stress in vertical direction. With increasing depth the magnitude of horizontal stress components and their influence would rise. Modelling approaches including considerations of the full stress tensor can be found in Greve and Blatter (2009), Salamantin et al. (2009) and Meyer and Hewitt (2017). It might be worthwhile to use the constitutive relation for grain boundary sliding by Alley (1987) in such a modelling context. This must not necessarily result in a full three dimensional model as the problem can be formulated axially symmetrical. This would require an adjustment of the constitutive relation. A more extensive interpretation of the factors obtained in the best matches is therefore challenging. The determination of a single factor C_v for one or all of the variants is not useful. It would not result in better simulation results compared to other published firn densification models. The site specific values of the factors, determined using the presented optimisation approach, simply show the differences in the variants of the constitutive relation.

6 Conclusions

Using variants of the constitutive relation for grain boundary sliding by Alley (1987) and a efficient optimisation scheme, we were able to reproduce 159 firn density profiles reasonably well. Thus we conclude, that the description of grain boundary sliding as introduced by Alley (1987) is appropriate for the simulation of firn densification at low density.

The modification of the constitutive relation by Bréant et al. (2017) leads to slightly better simulation results when the first stage of firn densification is considered solely. Further considerations including the transition from the first to the second stage had to answer the question in which domain and to which extent different processes driving the densification apply.

In our optimisation approach we use a single factor representing various model parameters and search for the factor value leading to the best match between simulated and measured firn profiles. In this way the site specific simulation results are independent of the possibly deficient, now collectively considered, model parameters. It is not possible to derive a distinct value for the factor representing the climatic conditions at all locations of the investigated firn profiles. The use of a global factor would lead to worse simulation results compared to existing firn density models. Rather we find a linear dependency of the factors on the surface mass balance specific to the location.

As the amount of surface accumulation affects the load situation, we assume it is not represented well in the model. Unlike other firn densification models, the physical approach of grain boundary sliding depends not directly on the surface mass balance, but on the actual stress. Further interpretation of the resulting factors is difficult using the presented simulation setup. The description of grain boundary sliding by Alley (1987) could benefit from a higher dimensional approach including horizontal components of the stress tensor. Modelling approaches of such kind include Greve and Blatter (2009), Salamantin et al. (2009), and Meyer and Hewitt (2017).

We want to emphasise, that any kind optimisation approaches are only possible due to enormous efforts of the SUMup team (Koenig and Montgomery, 2019), that made a vast amount of firn core data available. This is strategically crucial for firn densification modelling advances, which adds to the recommendations of FirnMICE (Lundin et al., 2017) for enhanced efforts for physically based models.

Code availability. The code used for the simulation of firn profiles will become available via github.com and gitlab.com at the time of publication of this manuscript.

Appendix A: Model description

A1 Numerical Treatment of Densification

All model equations are solved on an adapting one dimensional grid, updated in every time step. The approach follows the concept of an updated Lagrangian description with the update velocity of the grid being the material flow velocity. This results in material fixed coordinates. The Lagrangian like description allows for a very high spatial and temporal resolution in the simulations. It can be shown that integrating the local Eulerian form of the mass balance in one dimension over a material control volume with moving boundaries $z_1(t)$ and $z_2(t)$ leads to (Ferziger and Perić, 2002, p. 374):

$$\frac{d}{dt}\int\limits_{z_1(t)}^{z_2(t)} \rho\, dz + \int\limits_{z_1(t)}^{z_2(t)} \frac{\partial}{\partial z}\left(\rho\left(v - v_b\right)\right) dz = 0\,. \tag{A1}$$

Here ρ describes the density, z the vertical coordinate, t the time and v is the material flow velocity, whereas v_b represents the grid velocity or velocity of the integration boundary. When the grid velocity equals the material flow velocity $v_b = v$, the second part of Equation (A1), describing advection, vanishes. The resulting equation is equal to the Lagrangian form of the mass balance (Ferziger and Perić, 2002, p. 374). On a one dimensional grid, built up by a number of grid points, as illustrated in Fig. A1, we define the grid point velocity to be v_b and to equal the flow velocity $v_b \equiv v$. The location of all grid points is updated in every time step by integrating the grid point velocity v_b using a forward Euler scheme. In this way advection is entirely represented by the adapting grid.

The grid point velocity v_b is calculated using the constitutive equation of grain boundary sliding as described in Section 2.1 and the definition of the strain rate in one dimension. The description of grain boundary sliding provides the strain rate in vertical direction along the grid $\dot{\varepsilon}_{zz}$ as a function of the vertical stress σ_{zz}, density ρ, temperature T and grain radius r

$$\dot{\varepsilon}_{zz} = f\left(\sigma_{zz}, \rho, T, r\right) = \frac{\partial v}{\partial z} = \frac{\partial v_b}{\partial z}\,. \tag{A2}$$

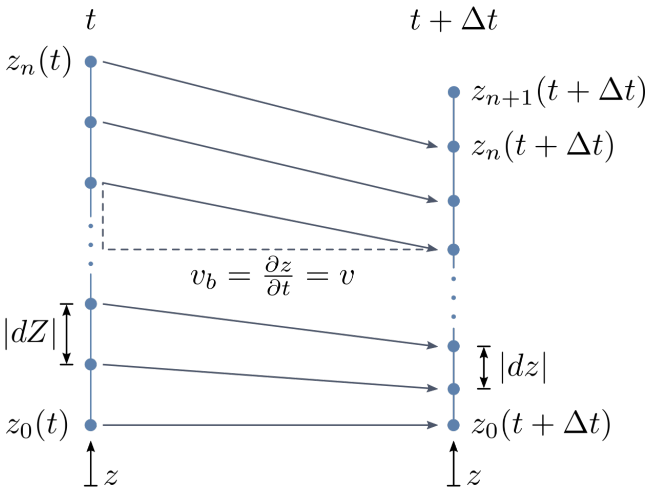

Figure A1. Principle of the grid evolution. On the left side a grid at time t is shown. The updated grid at time $t + \Delta t$ is illustrated on the right hand side of the figure. The grid points move with the grid point velocity v_b which equals to material flow velocity v. At time $t + \Delta t$ an additional grid point z_{n+1} representing accumulation is added. Distances between neighbouring grid points can be understood as material line elements $|dZ|$ and $|dz|$ in the reference and in the current configuration respectively.

The strain rate of a material line element can be defined as the spatial derivative of the velocity as shown in Equation (A2) (Haupt, 2002, pp. 32-38). On a one dimensional grid, defined by a number of grid points, the space between neighbouring grid points can be considered as a material line element (see Fig. A1). Therefore the grid point velocity v_b can easily be computed by integrating the strain rate $\dot{\varepsilon}_{zz}$ in vertical direction along the length of the grid cell:

$$v_b = \int\limits_{z_1}^{z_2} \dot{\varepsilon}_{zz}\, dz\,. \tag{A3}$$

For the implementation of Equation (A3) an integration constant determined by a suitable boundary condition is needed. It is reasonable to apply a Dirichlet boundary condition, forcing the grid point velocity v_b to be zero, at either the top or the base of the computational domain, representing a fixed reference point at the top or the base of the modelled firn profile, respectively. All other points defining the adapting grid are moving with respect to this anchor point. In case of the present study we decided to place the anchor point at the base of the simulated firn profiles (z_0 in Fig. A1). Depth coordinates of profiles shown in following figures were adjusted for better readability.

For the representation of accumulation at the top of a simulated firn profile an inflow boundary condition has to be implemented. To achieve this, in every time step an additional grid point is added at the top of the grid. Its coordinate within the grid $z_{n+1}(t + \Delta t)$ is calculated by

$$z_{n+1}(t + \Delta t) = z_n(t + \Delta t) + \Delta t\, a_0(t)\, \frac{\rho_{\text{water}}}{\rho_0}\,, \tag{A4}$$

with a_0 the accumulation rate given in $m\,s^{-1}$ water equivalent, Δt the length of the time step, ρ_{water} the density of water and ρ_0 the density of the deposited snow. The position of a new grid point ($z_{n+1}(t+\Delta t)$ in Fig. A1) is the position of the firn surface at the last time step z_n plus the thickness of the firn layer deposited during the last time step. This thickness is defined by the time time step Δt and the time dependent accumulation rate $a_0(t)$. As we use an accumulation rate given in the unit of meter water equivalent per second, it has to be converted to the unit of meter firn equivalent taking the site specific surface firn density ρ_0 and water density ρ_{water} into account.

This process results in a growing number of grid points. Therefore grid points are removed from the extending model domain at its base when a maximum number is reached.

A2 Stress

For the evaluation of the stress in vertical direction σ_{zz} we use the local form of the static linear momentum balance in its Eulerian description. We neglect the part of acceleration, as changes in velocity are assumed to be small, leading to

$$\frac{\partial \sigma_{zz}}{\partial z} + \rho g = 0. \tag{A5}$$

Computation of the stress σ_{zz} can easily be achieved by integrating the product of density ρ and acceleration due to gravity g along the simulated profile. We assume the surface of the profile to be traction free.

A3 Density

As pointed out in Section A1 and illustrated by Equation (A1) the change of the density integrated over a control volume with respect to time has to be zero. Or in other words, the mass incorporated in a control volume cannot change. As the position of the grid points, and therefore the material control volume, does change, the density is changing accordingly. The evaluation of the density integral over a control volume at two time steps leads to

$$\rho(t)\left(z_2(t) - z_1(t)\right) = \rho(t+\Delta t)\left(z_2(t+\Delta t) - z_1(t+\Delta t)\right). \tag{A6}$$

As the space between two neighbouring grid points can be understood as a material line element (Haupt, 2002, pp. 32-38), Equation (A6) can be rewritten in the form of Equation (A7). Where $|dZ| = |z_2(t) - z_1(t)|$ and $|dz| = |z_2(t+\Delta t) - z_1(t+\Delta t)|$ are the lengths of a material line element in the reference configuration and its image in the current configuration respectively:

$$\rho(t)|dZ| = \rho(t+\Delta t)|dz|. \tag{A7}$$

Sorting Equation (A7) leads to the formulation of the density change with respect to time depending on the definition of the strain ε_{zz} in one dimension (Haupt, 2002, p. 34)

$$\rho(t+\Delta t) - \rho(t) = -\rho(t+\Delta t)\left(\frac{|dz| - |dZ|}{|dZ|}\right) = -\rho\,\varepsilon_{zz}. \tag{A8}$$

The evolution of density can therefore be computed by integration of the strain rate $\dot{\varepsilon}_{zz}$ (Section 2.1) in time.

A4 Temperature

As pointed out in Section A1 all advection in the model domain is represented by the moving grid. Therefore the description of temperature evolution reduces to simple heat diffusion:

$$\rho c_p \left(\frac{\partial T}{\partial t}\right) + \frac{\partial}{\partial z}\left(k(\rho)\frac{\partial T}{\partial z}\right) = 0\,. \tag{A9}$$

Following Paterson (1994), we assume a constant heat capacity of $c_p = 2009\,\mathrm{J\,kg^{-1}\,K^{-1}}$ and following the example of Zwinger et al. (2007) a density dependent thermal conductivity, described by Sturm et al. (1997) as

$$k(\rho) = \left(0.138\,\mathrm{W\,m^{-1}\,K^{-1}}\right) - \left(1.010\times10^{-3}\,\mathrm{W\,m^{3}\,kg^{-1}\,K^{-1}}\right)\rho + \left(3.233\times10^{-6}\,\mathrm{W\,m^{5}\,kg^{-2}\,K^{-1}}\right)\rho^2\,. \tag{A10}$$

The temperature profile is initialised using a constant mean value computed from the site specific surface forcing. In order to solve for the temperature a Neumann boundary condition is used at the profile base. The first derivative of the temperature is forced to be zero.

A5 Grain Radius

Alley (1987) used measured grain size data to fit his simulation results to four firn profiles. As information about the grain size is sparse, we use a modelling approach for the description of the grain radius. The evolution of the grain radius r is simulated using the well known description of Stephenson (1967) and Gow (1969) as given in Arthern et al. (2010). Stephenson (1967) and Gow (1969) describe the grain size in means of the mean cross-sectional area. Arthern et al. (2010) however assume the mean cross-sectional area to be $A = (2/3)\pi r^2$ and formulate the grain growth rate as

$$\frac{\partial r^2}{\partial t} = k_0 \exp\left(-\frac{E_g}{RT}\right)\,. \tag{A11}$$

This formulation allows for simple calculation of the grain radius r. Values for activation energy $E_g = 42.4\,\mathrm{kJ\,mol^{-1}}$ and pre-factor $k_0 = 1.3\times10^{-7}\,\mathrm{m^2\,s^{-1}}$ of the Arrhenius law are based on data published in Paterson (1994) and were also adapted from Arthern et al. (2010). In contrast to Arthern et al. (2010) we do not use the mean annual temperature but the actual temperature $T(z,t)$ along the simulated profile. In order to solve Equation (A11), a suitable boundary conditions has to be provided. We chose to prescribe a constant surface grain radius. See Section 3.2 for further information on the boundary condition.

A6 Age

For reasons of comparison (Section 3.2) and general interest additionally the firn age χ is simulated. Again due to the fact that advection is represented by the adapting grid, the description is very simple. It is calculated from

$$\frac{\partial \chi}{\partial t} = 1\,. \tag{A12}$$

New deposited snow has an age of zero, prescribed in the form of a Dirichlet boundary condition. The age discretized at the grid points then increases according to the time step.

A7 Time Discretisation

Time is discretised using constant time steps. For this study 48 time steps per year have shown to be a good compromise between simulation costs and resolution and was used throughout all simulations. The grid resolution depends on the time step as a new grid point is generated in every time step representing accumulation as described in Section A1 and shown in Equation (A4). Time dependent properties such as the density, temperature, grain radius and age were developed using an explicit Euler scheme.

Author contributions. T.S. has developed the numerics, code, conducted and analysed all simulations. All authors have jointly developed the concept of the modelling approach, discussed the results and wrote the manuscript.

Competing interests. We declare that no competing interests are present.

Acknowledgements. This project has been funded by the German Research Foundation in the Priority Program SPP1158 under project number 403642112. We want to acknowledge the fantastic community effort SUMup, which provides a database of firn core data. We want to thank Sepp Kipfstuhl (AWI) and Johannes Freitag (AWI) for discussions on firn densification.

References

Alley, R. B.: Firn Densification by Grain-Boundary-Sliding: A First Model, Journal de Physique, 48, C1–249 – C1–256, https://doi.org/https://doi.org/10.1051/jphyscol:1987135, 1987.

Amante, C. and Eakins, B. W.: ETOPO1 1 Arc-Minute Global Relief Model: Procedures, Data Sources and Analysis, NOAA Technical Memorandum NESDIS NGDC-24, National Geophysical Data Center, NOAA, 2009.

Arnaud, L., Barnola, J. M., and Duval, P.: Physical modeling of the densification of snow/firn and ice in the upper part of polar ice sheets, Phyiscs of Ice Core Records, pp. 285–305, 2000.

Arndt, J. E., Schenke, H. W., Jakobsson, M., Nitsche, F. O., Buys, G., Goleby, B., Rebesco, M., Bohoyo, F., Hong, J., Black, J., Greku, R., Udintsev, G., Barrios, F., Reynoso-Peralta, W., Taisei, M., and Wigley, R.: The International Bathymetric Chart of the Southern Ocean (IBCSO) Version 1.0 - A new bathymetric compilation covering circum-Antarctic waters, Geophysical Research Letters, 40, 3111–3117, https://doi.org/https://doi.org/10.1002/grl.50413, 2013.

Arthern, R. J. and Wingham, D. J.: The Natural Fluctuations of Firn Densification and their Effect on the Geodetic Determination of Ice Sheet Mass Balance, Climatic Change, 40, 605–624, https://doi.org/https://doi.org/10.1023/A:1005320713306, 1998.

Arthern, R. J., Vaughan, D. G., Rankin, A. M., Mulvaney, R., and Thomas, E. R.: In situ measurements of Antarctic snow compaction compared with predictions of models, Journal of Geophysical Research, 115, https://doi.org/https://doi.org/10.1029/2009JF001306, 2010.

Bader, H.: Sorge's Law of Densification of Snow on High Polar Glaciers, Journal of Glaciology, 2, 319–323, https://doi.org/https://doi.org/10.3189/S0022143000025144, 1954.

Bréant, C., Marinterie, P., Orsi, A., Arnaud, L., and Landais, A.: Modelling firn thickness evolution during the last deglaciation: constraints on sensitivity to temperature and impurities, Clim. Past., 13, 833–853, https://doi.org/https://doi.org/10.5194/cp-13-833-2017, 2017.

Cuffey, K. M. and Paterson, W. S. B.: The Physics of Glaciers, Butterworth-Heinemann, fourth edition edn., 2010.

Ferziger, J. H. and Perić, M.: Computational Methods for Fluid Dynamics, Springer, Berlin, Heidelberg, New York, Barcelona, Hong Kong, London, Milan, Paris, Tokyo, 3., rev. edn., 2002.

Fourtenau, K., Gillet-Chaulet, F., Martinerie, P., and Faïn, X.: A Micro-Mechanical Model for the Transformation of Dry Polar Firn Into Ice Using the Level-Set Method, Front. Earth. Sci., 8, https://doi.org/https://doi.org/10.3389/feart.2020.00101, 2020.

Freitag, J., Kipfstuhl, S., Laepple, T., and Wilhelms, F.: Impurity-controlled densification: a new model for stratified polar firn, Journal of Glaciology, 59, 1163–1169, https://doi.org/https://doi.org/10.3189/2013JoG13J042, 2013.

Goujon, C., Barnola, J.-M., and Ritz, C.: Modeling the densification of polar firn including heat diffusion: Application to close-off characteristics and gas isotopic fractionation for Antarctica and Greenland sites, Journal of Geophysical Research, 108, 4792, https://doi.org/https://doi.org/10.1029/2002JD003319, 2003.

Gow, A. J.: On the Rates of Growth of Grains and Crystals in South Polar Firn, Journal of Glaciology, 8, 241–252, https://doi.org/https://doi.org/10.3189/S0022143000031233, 1969.

Greve, R. and Blatter, H.: Dynamics of Ice Sheets and Glaciers, Advances in Geophyiscal and Environmental Mechanics and Mathematics, Springer-Verlag, Berlin Heidelberg, https://doi.org/10.1007/978-3-642-03415-2, 2009.

Harper, J., Humphrey, N., Pfeffer, W. T., Brown, J., and Fettweis, X.: Greenland ice-sheet contribution to sea-level rise buffered by meltwater storage in firn, Nature, 491, 240–243, https://doi.org/https://doi.org/10.1038/nature11566, 2012.

Haupt, P.: Continuum Mechanics and Theory of Materials, Springer-Verlag Berlin Heidelberg New York, 2002.

Herron, M. M. and Langway, C. C.: Firn Densification: An Empirical Model, Journal of Glaciology, 25, 373–385, https://doi.org/https://doi.org/10.3189/S0022143000015239, 1980.

Hersbach, H., Bell, B., Berrisford, P., Hirahara, S., Horányi, A., Muñoz Sabater, J., Nicolas, J., Peubey, C., Radu, R., Schepers, D., Simmons, A., Soci, C., Abdalla, S., Abellan, X., Balsamo, G., Bechtold, P., Biavati, G., Bidlot, J., Bonavita, M., De Chiara, G., Dahlgren, P., Dee, D., Diamantakis, M., Dragani, R., Flemming, J., Forbes, R., Fuentes, M., Geer, A., Haimberger, L., Healy, S., Hogan, R. J., Hólm, E., Janisková, M., Keeley, S., Laloyaux, P., Lopez, P., Lupu, C., Radnoti, G., de Rosnay, P., Rozum, I., Vamborg, F., Villaume, S., and Thépaut, J.-N.: The ERA5 gloabal reanalysis, Quarterly Journal of the Royal Meterological Society, 146, 1999–2049, https://doi.org/https://doi.org/10.1002/qj.3803, 2020.

Ignat, M. and Frost, H. J.: Grain Boundary Sliding in Ice, J. Phys. Colloques, 48, C1–189–C1–195, https://doi.org/https://doi.org/10.1051/jphyscol:1987127, 1987.

Itagaki, K.: Self-Diffusion in Single Crystals of Ice, Journal of the Physical Society of Japan, 19, 1081, https://doi.org/https://doi.org/10.1143/JPSJ.19.1081, 1964.

Johnson, J. B. and Hopkins, M. A.: Identifying microstructural deformation mechanisms in snow using discrete-element modeling, Journal of Glaciology, 51, 432–442, https://doi.org/https://doi.org/10.3189/172756505781829188, 2005.

Kinosita, S.: Compression of Snow at Constant Speed, Physics of Snow and Ice: proceedings, 1, 911–927, International Conference on Low Temperature Science. I. Conference on Physics of Snow and Ice, II. Conference on Cryobiology. (August 14-19, 1966, Sapporo, Japan), 1967.

Koenig, L. and Montgomery, L.: Surface Mass Balance and Snow Depth on Sea Ice Working Group (SUMup) snow density subdataset, Greenland and Antarctica, 1950-2018, Tech. rep., Arctic Data Center, https://doi.org/doi:10.18739/A26D5PB2S, 2019.

Ligtenberg, S. R. M., Helsen, M. M., and van den Broeke, M. R.: An improved semi-empirical model for the densification of Antarctic firn, The Cryosphere, 5, 809–819, https://doi.org/https://doi.org/10.5194/tc-5-809-2011, 2011.

Linow, S., Hörhold, M. W., and Freitag, J.: Grain-size evolution of polar firn: a new empirical grain growth parameterization based on X-ray microcomputer tomography measurements, Journal of Glaciology, 58, 1245–1252, https://doi.org/https://doi.org/10.3189/2012JoG11J256, 2017.

Lundin, J. M. D., Stevens, C. M., Arthern, R., Buizert, C., Orsi, A., Ligtenberg, S. R. M., Simonsen, S. B., Cummings, E., Essery, R., Leahy, W., Harris, P., Helsen, M. M., and Waddington, E. D.: Firn Model Intercomparison Experiment (FirnMICE), Journal of Glaciology, 63, 401–422, https://doi.org/https://doi.org/10.1017/jog.2016.114, 2017.

Maeno, N. and Ebinuma, T.: Pressure Sintering of Ice and Its Implications to the Densification of Snow at Polar Glaciers and Ice Sheets, J. Phys.Chem., 87, 349–365, https://doi.org/https://doi.org/10.1021/j100244a023, 1983.

Meyer, C. R. and Hewitt, I. J.: A continuum model for meltwater flow through compacting snow, The Cryosphere, 11, 2799–2813, https://doi.org/https://doi.org/10.5194/tc-11-2799-2017, 2017.

Miller, H. and Schwager, M.: Accumulation rate and stable oxygen isotpoe ratios of ice core ngt03C93.2 form the North Greenland Traverse, PANGAEA, https://doi.org/https://doi.org/10.1594/PANGAEA.218274, 2004.

Morris, E. M., Muvaney, R., Arthern, R. J., Davies, D., Gurney, R. J., Lambert, P., De Rydt, J., Smith, A. M., Tuckwell, R. J., and Winstrup, M.: Snow Densification and Recent Accumulation Along the iSTAR Traverse, Pine Island Glacier, Antarctica, Journal of Geophysical Reasearch: Earth Surface, 122, 2284–2301, https://doi.org/https://doi.org/10.1002/2017JF004357, 2017.

Muñoz Sabater, J.: ERA5-Land monthly averaged data from 1981 to present, Tech. rep., Copernicus Climate Change Service (C3S) Climate Data Store (CDS), https://doi.org/10.24381/cds.68d2bb3, accessed on 30-08-2021, 2019.

Noël, B., van de Berg, W. J., van Meijgaard, E., Kuipers Munneke, P., van de Wal, R. S. W., and van den Broeke, M. R.: Evaluation of the updated regional climate model RACMO2.3: summer snowfall impact on the Greenland Ice Sheet, The Cryosphere, 9, 1831–1844, https://doi.org/https://doi.org/10.5194/tc-9-1831-2015, 2015.

Orsi, A. J., Kawamura, K., Masson-Delmotte, V., Fettweis, X., Box, J. E., Dahl-Jensen, D., Clow, G. D., Landais, A., and Severinghaus, J. P.: The recent warming trend in North Greenland, Geophysical Research Letters, 44, 6235–6243, https://doi.org/https://doi.org/10.1002/2016GL072212, 2017.

Paterson, W. S. B.: The Physics of Glaciers, Butterworth-Heinemann, Linacre House, Jordan Hill, Oxford OX2 8DP, 200 Wheeler Road, Birlington, MA 01803, 3rd edn., 1994.

Raj, R. and Ashby, M. F.: On Grain Boundary Sliding and Diffusional Creep, Metallurgical Transactions, 2, 1113–1127, https://doi.org/https://doi.org/10.1007/BF02664244, 1971.

Robin, G. d. Q.: Glaciology III: Seismic Shooting and Related Investigations, Norwegian-British-Swedish Antarctic Expedition, 1949-52, Scientific Results Vol. 5, Norsk Polarinstitutt, Oslo, 1958.

Roscoat, S. R. d., King, A., Phillip, A., Reischig, P., Ludwig, W., Flin, F., and Meyssonnier, J.: Analysis of Snow Microstructure by Means of X-Ray Diffraction Contrast Tomography, Advanced Engineering Materials, 13, 128–135, https://doi.org/https://doi.org/10.1002/adem.201000221, 2010.

Salamantin, A. N., Lipenkov, V. Y., Barnola, J. M., Hori, A., Duval, P., and Hondoh, T.: Snow/Firn Densification in Polar Ice Sheets, in: Physics of Ice Core Records II: Papers collected after the 2nd International Workshop on Physics of Ice Core Records, held in Sapporo, Japan, 2-6 February 2007, edited by Hondoh, T., pp. 195–222, 2009.

Simonsen, S. B., Stenseng, L., Aðalsgeirsdóttir, G., Faustio, R. S., Hvidberg, S., and Lucas-Picher, P.: Assessing a multilayered dynamic firn-compaction model for Greenland with ASIRAS radar measurement, Journal of Glaciology, 59, 545–558, https://doi.org/https://doi.org/10.3189/2013JoG12J158, 2013.

Stephenson, P. J.: Some Considerations of Snow Metamorphism in the Antarctic Ice Sheet in the Light of Ice Cycle Studies, in: Physics of Snow and Ice, edited by Ōura, H., vol. 1, Part2, pp. 725–740, Hokkaido University, Institute of Low Temperature Science, Sapporo, 1967.

Sturm, M., Holmgren, J., König, M., and Morris, K.: The thermal conductivity of seasonal snow, Journal of Glaciology, 43, 26–41, https://doi.org/https://doi.org/10.3189/S0022143000002781, 1997.

Székely, G. J., Rizzo, M. L., and Bakirov, N. K.: Measuring and testing dependence by correlation of distances, The Annals of Statistics, 35, 2769–2794, https://doi.org/http://dx.doi.org/10.1214/009053607000000505, 2007.

Theile, T., Löwe, H., Theile, T. C., and Schneebeli, M.: Simulating creep of snow based on microstructure and the anisotropic deformation of ice, Acta Materialia, 59, 7104–7113, https://doi.org/https://doi.org/10.1016/j.actamat.2011.07.065, 2011.

Van Wessem, J. M., Reijmer, C. H., Morlighem, M., Mouginot, J., Rignot, E., Medley, B., Joughin, I., Wouter, B., Depoorter, M. A., Bambler, J. L., Lenaerts, J. T. M., Van De Berg, W. J., Van Den Broeke, M. R., and Van Meujgaard, E.: Improved representation of East Antarctic surface mass balance in a regional atmospheric climate model, Journal of Glaciology, 60, 761–770, https://doi.org/https://doi.org/10.3189/2014JoG14J051, 2014.

Vandecrux, B., Colgan, W., Solgaard, A. M., Steffensen, J. P., and Karlsson, N. B.: Firn Evoluation at Camp Century, Greenland: 1966–2100, Frontiers in Earth Science, 9, 1–16, https://doi.org/https://doi.org/10.3389/feart.2021.578978, 2021.

Wilhelms, F.: Density of ice core ngt03C93.2 from the North Greenland Traverse, Pangaea, https://doi.org/https://doi.org/10.1594/PANGAEA.56560, 2000.

Zwinger, T., Greve, R., Gagliardini, O., Shiraiwa, T., and Lyly, M.: A full Stokes-flow thermo-mechanical model for firn and ice applied to the Gorshkov crater glacier, Kamchatka, Annals of Glaciology, 45, 29–37, https://doi.org/https://doi.org/10.1029/2006JF000576, 2007.